Large-Scale Simulations for Understanding Surface Optical Spectra

W.G. Schmidt, A. Hermann, F. Fuchs, and M. Preuss

Computational Materials Science Group
Friedrich-Schiller-Universität
Max-Wien-Platz 1, 07743 Jena, Germany
wgs@ifto.physik.uni-jena.de

Summary. Surface optical spectroscopies are non-destructive and capable of operation within a wide range of environments. Their potential for materials characterization can only be exploited fully, however, when the physical mechanisms giving rising to optical features are well understood. Here we use large-scale numerical simulations to investigate two highly relevant and at the same time prototypical cases from *first principles*: (i) the origin of the optical anisotropy oscillations accompanying the thermal oxidation of Si(001) and (ii) the modification of the Si(001) surface optical response upon adsorption of 9,10-phenanthrenequinone. It is demonstrated to what extent strain, molecular transitions and adsorption-modified Si bulk wave functions contribute to the surface optical anisotropy.

1 Introduction

Optical spectroscopies are extremely valuable for the *in situ*, non-destructive and real-time surface monitoring under challenging conditions as may be encountered, e.g., during epitaxial growth. Reflectance anisotropy spectroscopy (RAS) is one of the plethora of surface sensitive spectroscopies probing linear optical coefficients which has been particularly successful in exploring surface structures. However, reliable calculations of the surface optical response are needed to fully exploit its diagnostic potential. The anisotropy of the reflectivity R of light polarized in two perpendicular directions in the surface plane, x and y, is given by [1, 2]

$$\frac{\Delta R}{R}(\omega) \equiv 2\frac{R_x - R_y}{R_x + R_y}(\omega) = \frac{16\pi\omega}{c}\Im\left\{\frac{\alpha_{xx}^{hs}(\omega) - \alpha_{yy}^{hs}(\omega)}{\epsilon_b(\omega) - 1}\right\}. \tag{1}$$

Here $\alpha_{ii}^{hs}(\omega)$ with $i = x, y$ is the diagonal tensor component of the averaged half-slab polarisability and $\epsilon_b(\omega)$ denotes the bulk dielectric function.

In this article we compare measured and calculated (according to Eq. 1) RAS spectra in order to better understand the physics and optical fingerprints of Si oxidation and the influence of thin organic layers on the optical properties of semiconductors.

2 Computational Method

The calculations are based on density functional theory (DFT) [3] which states that the ground-state energy E_0 of a N-electron system in an external potential $v_{ext}(\mathbf{r})$ is an unique functional of the ground-state electron density $n(\mathbf{r})$:

$$E_0[n] = T_s[n] + \int d^3r\, v_{ext}(\mathbf{r}) n(\mathbf{r}) + \frac{1}{2} \iint d^3r\, d^3r' \, \frac{n(\mathbf{r}) n(\mathbf{r}')}{|\mathbf{r} - \mathbf{r}'|} + E_{xc}[n]. \quad (2)$$

The functionals $T_s[n]$ and $E_{xc}[n]$ give the single-particle kinetic and the exchange-correlation energy of a N-electron system of density $n(\mathbf{r})$, respectively. The two other contributions to E_0 are the energy of the electrons in the external potential and the Hartree energy.
For a given external potential $v_{ext}(\mathbf{r})$ the functional $E_0[n]$ is minimized at the density $n_0(\mathbf{r})$ of the correct ground state. This variational property leads to an one-particle equation, the Kohn-Sham equation, that maps the many-electron problem onto a system of non-interacting electrons $\{\psi_i\}_i^N$ that has the same ground state density [4]:

$$\left\{ -\frac{\hbar^2}{2m} \nabla^2 + v_{ext}(\mathbf{r}) + v_H(\mathbf{r}) + v_{xc}(\mathbf{r}) \right\} \psi_i(\mathbf{r}) = \varepsilon_i \psi_i(\mathbf{r}), \quad (3)$$

$$n(\mathbf{r}) = \sum_{i=1}^{N} |\psi_i(\mathbf{r})|^2. \quad (4)$$

The terms $v_H(\mathbf{r})$ and $v_{xc}(\mathbf{r}) = \delta E_{xc}/\delta n(\mathbf{r})$ represent the Hartree and the exchange-correlation potential, respectively. By solving equations (3) and (4) self-consistently, one obtains the exact ground state density $n_0(\mathbf{r})$ and thus all physical properties that are functionals of this density.

For the numerical solution we expand the wave functions and potentials into plane waves $\psi_i(\mathbf{r}) \equiv \psi_{n\mathbf{k}}(\mathbf{r}) = \sum_{\mathbf{G}} c_{n\mathbf{k}}(\mathbf{G}) e^{i(\mathbf{k}+\mathbf{G})\mathbf{r}}$. This leads to very efficient algorithms for periodic systems, because it renders the kinetic energy operator diagonal and symmetries in reciprocal space can be exploited. The convergence is easily controlled by adjusting the energy cutoff of the plane-wave components in the basis.

The representation of the rapid oscillations of the wave functions near the nuclei demands many plane waves. However, it is the interstitial region that determines most of the interesting physical properties. There the wave functions are rather smooth and can be described by comparatively few plane waves. We therefore employ the Projector Augmented Wave (PAW) method [5], which establishes a one-to-one relation between the exact wave functions and a set of smooth pseudo wave functions, that match the exact ones outside a certain radius around each nucleus. The connection is mediated by a set of one-center projector functions $\{|p_j\rangle\}$. The Kohn-Sham equations for the plane wave coefficients $c_{n\mathbf{k}}(\mathbf{G})$ then read [6]

$$\sum_{\mathbf{G}'} \left\{ \frac{\hbar^2(\mathbf{k}+\mathbf{G})^2}{2m}\delta_{\mathbf{G}\mathbf{G}'} + V_{eff}(\mathbf{G}-\mathbf{G}') + \sum_{ij} p_{i\mathbf{k}}(\mathbf{G}) D_{ij} p^*_{j\mathbf{k}}(\mathbf{G}') \right\} c_{n\mathbf{k}}(\mathbf{G}')$$
$$= \sum_{\mathbf{G}'} \varepsilon_{n\mathbf{k}} \langle \mathbf{k}\mathbf{G} | S | \mathbf{k}\mathbf{G}' \rangle c_{n\mathbf{k}}(\mathbf{G}') \tag{5}$$

whith

$$V_{eff}(\mathbf{G}-\mathbf{G}') = \langle \mathbf{k}\mathbf{G} | V_{eff} | \mathbf{k}\mathbf{G}' \rangle, \quad p_{j\mathbf{k}}(\mathbf{G}) = \langle \mathbf{k}\mathbf{G} \,|\, p_j \rangle. \tag{6}$$

Here V_{eff} are the Fourier components of the effective local potential (containing v_{ext}, v_H and v_{xc}), $|p_j\rangle$ the projector functions and D_{ij} are the components of the non-local potential localized around the nuclei.

$$S = 1 + \sum_{ij} |p_i\rangle Q_{ij} \langle p_j| \tag{7}$$

is the overlap operator of the projector functions. The Kohn-Sham equations are thus rewritten as a generalized eigenvalue problem. Since the non-local parts of the Hamilton operator and the overlap operator have the same structure, the problem at hand can be solved very efficiently using iterative methods. The diagonalization of equation (5) can be efficiently parallelized, since it is diagonal in the index n of the eigenstate ("inter-band distribution"); furthermore, if there are enough nodes available, the diagonalization for the n-th state may be parallelized as well ("intra-band distribution"). However, each node must provide enough memory to store the total charge density given on a real-space mesh and the calculated wave functions. Since the orthogonalization of the eigenstates requires redistribution of the wave functions between all nodes, communication and latency become issues.

We use the DFT-PAW implementation in the Vienna Ab-initio Simulation Package (VASP) [7], together with the gradient-corrected parametrization of the exchange-correlation energy [8, 9]. The Kohn-Sham matrix is diagonalized using the Residual Minimization Method with Direct Inversion in Iterative Subspace (RMM-DIIS) [10]. This scheme is preferred over the more common Conjugate Gradient (CG) method, since the latter requires explicit orthonormalization of the search vector for each wave function with respect to all other wave functions during each iteration step, an $\mathcal{O}(N^3)$ operation. The RMM-DIIS scheme reduces the number of $\mathcal{O}(N^3)$ operations to a minimum [7]. Parallelization is done using the Message Passing Interface (MPI).

The surface systems are modeled using periodically repeated slabs. Each slab consists of 12 layers of Si covered with oxygen or an organic layer on both sides, and at least 10 Å of vacuum to avoid direct interaction of adjacent slabs. Within the surface plane we use a $p(4 \times 2)$ surface supercell. Brillouin zone integrations are performed on regular meshes in reciprocal space [11], corresponding to 64 k points in the (1×1) surface Brillouin zone. Wave functions are expanded into plane waves up to a cutoff energy of 400 eV (340 eV)

for oxidized (organic adlayer covered) surfaces. Relaxations of ionic positions are carried out using conjugate gradient or quasi-Newton algorithms, until the Hellmann-Feynman forces fall below 5 meV/Å (10 meV/Å). For optical properties we calculate the transition matrix elements from all-electron wave functions at an equivalent of 256 k points in the (1×1) surface Brillouin zone. The half-slab polarizabilities are then calculated in independent-particle approximation, but applying a scissors operator shift of $\Delta E = 0.5$ eV to account for the DFT band gap underestimation.

A large part of our calculations were carried out on a Cray T3E or a Cray

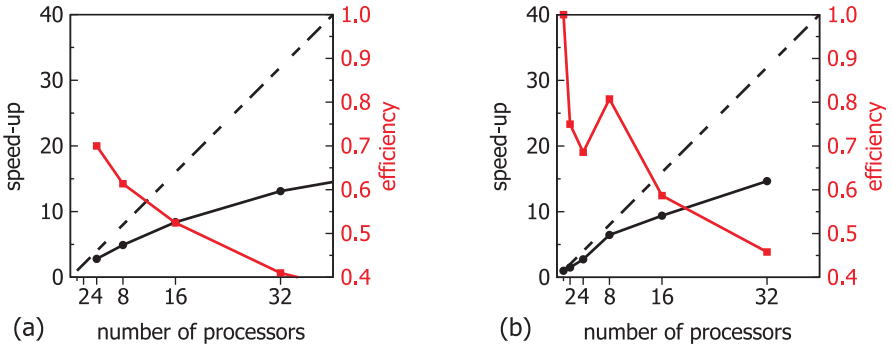

Fig. 1. Speedup and efficiency for (a) Cray T3E, and (b) Cray Opteron cluster.

Opteron cluster. Figure 1 shows the scaling behavior of our code on both systems. The efficiency is slightly better on the Opteron cluster than on the T3E, but both show significant loss due to overhead when using more than 16 processors. The systems we treat are rather large. The T3E has only 128 MB memory per processor, so we are forced to use more than 32 processors to handle our systems. The Opteron cluster, on the other hand, comes with 2 GB memory per processor, so we can exploit its good scaling behavior by using 4 to 8 processors per job. Typical job run times are 12 to 48 wall clock hours.

3 Results

3.1 Optical anisotropy of oxidized Si(001) surfaces

Despite decades of effort, the mechanism of the Si(001) surface oxidation as well as the microscopic structure of the silicon/silicon oxide interface are still under discussion, see, e.g, Ref. [12]. Photons penetrate deeply into the substrate, of the order of 10^3 Å, and could thus be helpful to explore the oxidation process, even far below the surface. RAS spectra measured during thermal

oxide growth show oscillations, i.e, repeated changes of the optical anisotropy polarity, for photon energies around the E_1 and E_2 critical points (CPs) of bulk Si as well as above 5 eV [13, 14]. Scanning reflection electron microscopy [15] and total-energy calculations [16] indicate that the thermal oxidation of Si(001) proceeds layer-by-layer. This suggests to relate the optical anisotropy oscillations to the layer oxidation. However, previous numerical simulations based on ordered oxidized Si(001) surfaces [17, 18, 19, 20] failed to explain the measured data and their relation to the interface structure.

Figures 2 (iv) and (iii) show schematically the clean Si(001) surface and an energetically favored geometry used to model the oxidation of the first Si layer [21], respectively. The bottom curve in Fig. 2 shows the reflectance anisotropy calculated for the clean Si(001)$c(4\times2)$ surface. It is characterized by a strong, dimer-state related minimum at 1.7 eV. An additional minimum/maximum structure slightly below/above the E_1/E_2 CP energy of bulk Si at 3.5/4.3 eV results from surface-modified bulk states. The calculated spectrum agrees with the data measured for highly oriented, single-domain Si(001) surfaces [22, 23].

Upon oxidation, the reflectance anisotropy of the clean surface changes strongly. The 1.7 eV feature is quenched, due to the saturation of the Si-dimer states. In Fig. 2 we show the measured RAS data assigned to the complete oxidation of the first atomic monolayer [13]. It is positive for all photon energies considered, with maxima close to the E_1 and E_2 CPs and at about 5.3 eV. RAS calculations based on translationally invariant models of oxidized Si(001) surfaces only explain part of the measured features. The oxidation model shown in Fig. 2 (iii) gives rise to an optical anisotropy that is positive throughout the energy range probed. However, there are clear deviations between experiment and theory. The discrepancies between experiment and theory are even more pronounced for RAS calculations based on ordered surface structures different from the model shown in Fig. 2 (iii) [18, 19, 20].

The top curve in Fig. 2 shows experimental data assigned to the oxidation of the second monolayer [13]. Nearly an inversion of the signal is observed, compared to the spectrum assigned to the oxidation of the first monolayer (this inversion occurs repeatedly during the progression of the oxidation, see Ref. [14]). Negative anisotropies occur for photon energies close to the Si bulk CPs and above 4.5 eV. We failed completely to reproduce this spectrum using any of the structural models proposed for oxidation of the uppermost two atomic layers of Si(001) [21]. Strong deviations from experiment occur in all cases.

Surface disorder not contained in the translationally invariant oxidation models could possibly explain the failure of the calculations. That oxidation causes considerable surface disorder is in accord with high-energy electron diffraction data [15] and scanning tunneling microscopy images of Si(001) surfaces exposed to oxygen [24]. Bulk Si is optically isotropic. If the disorder of the oxide film above the interface renders this film optically isotropic too,

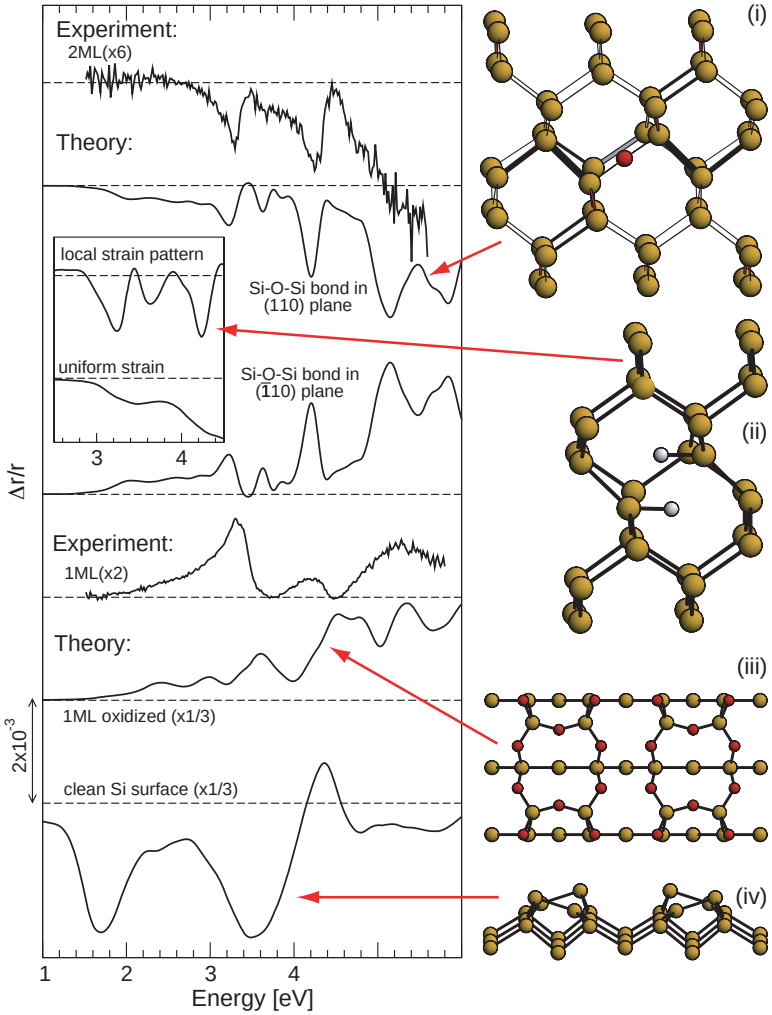

Fig. 2. RAS spectra $[Re\{(r_{[\bar{1}10]} - r_{[110]})/\langle r\rangle\}]$ calculated for the clean and oxidized Si configurations shown in the right panel (see text) are compared with measured data [13]. Dark yellow (red, white) symbols indicate Si (O, H) atoms.

the only source of optical anisotropy are oxygen atoms inserted into Si-Si bulk bonds directly at the interface. Therefore, the optical anisotropy induced by oxygen inserted into bulk Si bonds is investigated, using an orthorhombic supercell with 2×2×20 periodicities along the [$\bar{1}$10], [110], and [001] directions, respectively. The difference of the [$\bar{1}$10] and [110] bulk polarizability components is normalized such as to compare with the surface reflectance anisotropy. The results for Si-O-Si bonds in ($\bar{1}$10) and (110) planes (shown in

Fig. 2) reproduce the major features measured after oxidation of the first and second monolayer, respectively. Given the simplicity of this idealized model, the agreement between calculation and measurement is impressive. The measured RAS oscillations are thus explained naturally by assuming that (i) the oxidation occurs layer-by-layer and (ii) the silicon oxide directly above the abrupt interface is disordered and therefore optically isotropic.

After having reproduced the experimental data by calculations for oxidized Si bulk, we investigate the origin of the optical anisotropies in more detail. Earlier measurements of the Si-SiO_2 interface optical properties have often been interpreted in terms of strain-induced shifts of the Si bulk CP energies. We perform model calculations for bulk Si uniformly strained by 2% along [110], a value that roughly accounts for the lattice compression around an oxygen atom inserted into a Si(001)(2×2) interface unit cell. As seen in the inset of Fig. 2 (left panel), the optical anisotropy induced by such a macroscopic strain accounts for the sign and roughly for the magnitude of the measured signal, but does not reproduce the line shape. Therefore, either the Si-O bond-related electronic states or the complicated local deformation pattern must cause the peculiar features at E_1 and E_2. Based on a detailed analysis of the transition matrix elements contributing to the total RAS signal, we can exclude the first possibility: The optical anisotropies are caused be a multitude of perturbed Si bulk states. To corroborate the second hypothesis we perform calculations using the frozen lattice deformation pattern around an inserted oxygen, but replacing the O atom with two H atoms for Si dangling bond termination (see Fig. 2 (ii) and "local strain pattern" curve). Indeed, a line shape is obtained that agrees well with the oxygen inserted case, at least around E_1 and E_2. This shows that the strain is indeed causing the optical anisotropy. However, it is important to account for the *local* deformation pattern around the defect. An uniform compression is not sufficient to model the measured RAS. Figure 2 (i) illustrates the complexity of the Si bulk deformation around an oxidized Si bond. Here compressive and tensile strain is indicated by dark and light gray bonds, respectively, with the thickness of the bonds indicating the amount of local strain.

3.2 Si(001) surface optical anisotropies induced by PQ molecules

In the last years, an increasing amount of work has been dedicated to the grafting of organic molecules on the Si(001) surface. Such hybrid systems open the way for integrating the electronic, optical or biological properties of organic layers in classical silicon-based devices. The structural investigation of these systems by the usual laboratory surface techniques using electrons is difficult, because the direct access to the interface is prevented by the presence of the organic adlayer. In contrast, techniques based on photons can be used to study the interface through the adsorbed thin film. Presently, however, the contribution of organic thin films to the semiconductor surface

optical response is essentially unknown, hindering the efficient use of optical spectroscopies for organic layer and interface characterization.

Recently, Hacker and Hamers [25] studied the optical anisotropy of 9,10-phenanthrenequinone ("PQ", $C_{14}O_2H_8$) adsorbed on Si(001) as a prototype for a π-conjugated overlayer system. PQ has two highly reactive carbonyl groups assumed to bond to the surface ("bonding group"), a delocalized π-electron system ("functional group"), and forms a large variety of derivates. The π-conjugation, likely to remain intact upon adsorption, should allow for direct observation of intramolecular as well as interface- and substrate-related transitions in the experimentally accessible photon energy range. Indeed, a pronounced RAS feature was measured for photon energies of about 5.2 eV and assigned to intramolecular $\pi - \pi^*$ transitions. Here we use the adsorption of PQ to analyze in detail the optical response of an organic monolayer on Si(001).

Experiment [26] and total-energy calculations [27] indicate that the molecules bond via their carbonyl groups to the Si dimer, forming a [4+2] Diels-Alder product. The optimized geometry is shown in Fig. 3 (i). It features PQ molecules that arrange in zig-zag chains on the surface and co-adsorbed hydrogen at the remaining Si dimer atoms. This configuration is used below for optical-response calculations.

The reflectance anisotropy calculated for PQ molecules adsorbed on Si(001) (solid curve in Fig. 3) is in good agreement with the measured data [25]. Compared to the spectrum of the clean surface (see, e.g., Refs. [22, 23]), new optical anisotropies show up. Among these, the B_1 feature at about 5.2 eV is the most pronounced one.

In order to determine the origin of these interface optical anisotropies, the valence orbitals of the supercell are classified with respect to their localization either below or above the Si surface. This decomposition allows for the separation of the substrate and organic layer contributions to the total optical signal. The respective RAS spectra are shown by the dashed lines in Fig. 3. Obviously, bulk contributions dominate the optical signal. The RAS features at the E_1 and E_2 Si bulk critical points as well as the B_1 and B_2 features arise from transitions involving Si bulk states. This is in clear contrast to the interpretation of the B_1 feature as due to molecular $\pi - \pi^*$ transitions [25]. Therefore, we perform additional calculations: The adsorbed PQ molecules are replaced by two OH groups each (cf. Fig. 3 (ii)). By keeping the slab geometry (including the O atoms) fixed, the RAS contribution of the strained and rebonded substrate can be calculated. The obtained spectrum (bottom curve in Fig. 3) reproduces all main features of the Si substrate signal, i.e., the E_1/E_2 features as well as B_1 and B_2. Evidently, B_1 and B_2 do not arise from molecular transitions but are clearly due to adsorption-induced distortions of the substrate. We find that both the adsorption-induced strain in the silicon lattice and the formation of Si-O bonds contribute to these anisotropies.

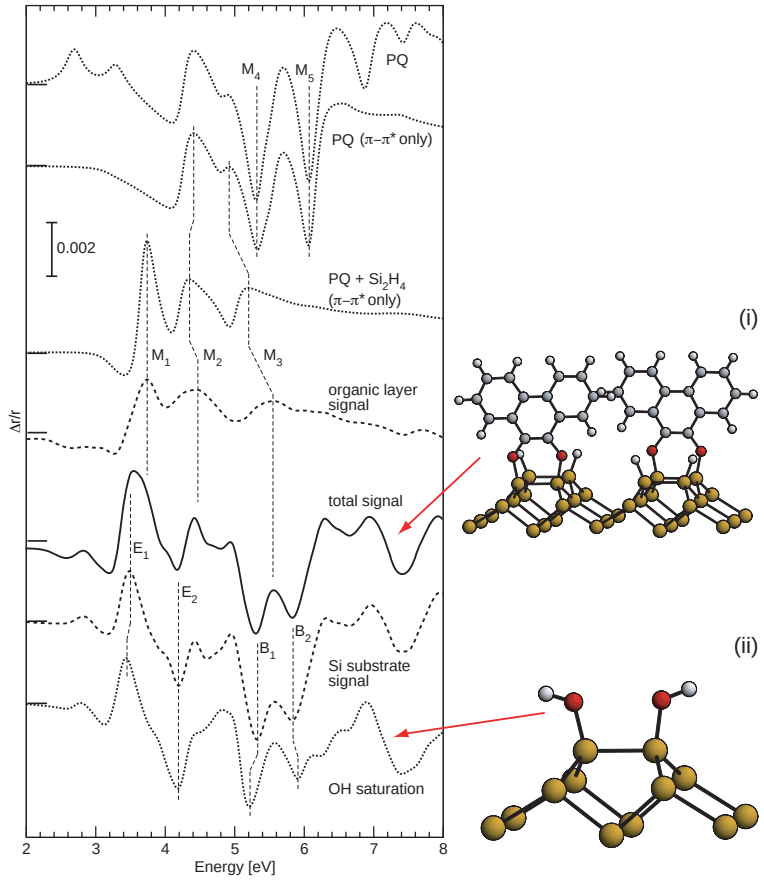

Fig. 3. Total calculated RAS spectrum $[Re\{(r_{[\bar{1}10]} - r_{[110]})/\langle r\rangle\}]$ and its decomposition into overlayer and bulk contributions (see text). The side panel shows (i) the structural model for PQ adsorption on Si(001) and (ii) a model where PQ molecules have been substituted by OH groups (see text). Large (dark, grey, light) circles denote Si (O, C, H) atoms, respectively.

Although less pronounced than expected, there are also RAS contributions to the total signal that originate in the organic layer as shown in Fig. 3: The total signal is modified by molecular transitions denoted M_1, M_2, and M_3. What is the origin of these features? To answer this question we simulate the RAS response of an organic overlayer on top of optically isotropic Si by using the three-layer model shown in the inset of Fig. 4. This model allows for simulating the optical response as a function of the organic layer constituents.

The topmost RAS curve in Fig. 3 is obtained by assuming the organic layer to consist of PQ molecules that have an optical absorption equal to

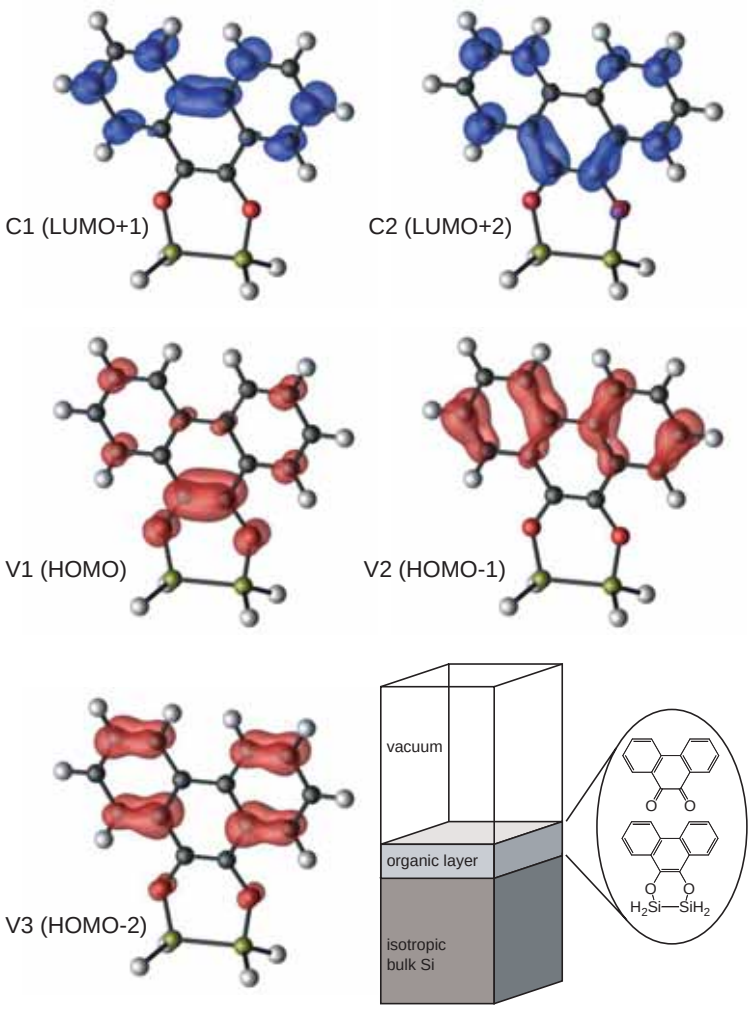

Fig. 4. Relevant molecular orbitals of the PQ+Si_2H_4 molecule (see text). The three-layer model for simulating "simplified" RAS spectra is shown as inset.

their gas-phase spectrum. Interestingly, the calculated RAS spectrum shows pronounced π-π^* transition-related M_4 and M_5 features that nearly coincide in energy with the B_1 and B_2 peaks measured by Hacker and Hamers [25]. However, the RAS obtained from the fictitious layer of gas-phase PQ molecules clearly fails to reproduce the calculated organic layer contribution to the total signal (upper dashed curve in Fig. 3). This is expected: The carbonyl group-related transitions will vanish or at least be shifted to much higher energies upon molecular adsorption.

Therefore, in a second step, we calculate the RAS as above, but restrict the optical response to π-π^* transitions of the gas-phase molecule. The result, however, agrees only slightly better with the organic layer contribution to the total RAS.

To model the bonding with the Si substrate, we therefore construct in a third step an artificial PQ+Si_2H_4 molecule (see Fig. 4), using the atomic coordinates from the calculated adsorption geometry. The Si-O bonding leads to a charge redistribution in the molecule and to the formation of a new C=C double bond (V1 in Fig. 4) between the carbonyl group C atoms, which corresponds now to the highest occupied molecular orbital. By restricting the calculation to transitions between the three highest occupied π orbitals and the two lowest unoccupied π^* orbitals one obtains the third curve of Fig. 3. Obviously, the line shape and peak positions of the organic layer signal are well described by such a model for the constituents of the organic film.

Thus, the essential parts of the molecular contributions to the RAS can be traced back to a few π-π^* transitions within the PQ molecule. However, the bonding to the substrate must be taken into account: The feature M_1 arises solely from transitions involving the C=C double bond which forms as a result of the [4+2] Diels-Alder reaction with the Si=Si dimer. At the same time, the formerly pronounced M_4 and M_5 features are strongly reduced in amplitude and shifted in energy, due to the substrate-bonding related changes of the respective molecular orbitals. Fig. 4 shows the molecular states responsible for the RAS features related to the organic overlayer: M_1, M_2, and M_3 stem from $V_1 - C_2$, $V_2 - C_1$, and $V_3 - C_1$ transitions, respectively.

4 Conclusions

In conclusion, we calculated the optical response of clean, oxidized as well as organically modified Si(001) surfaces from *first principles*.

Comparison of the simulated optical spectra with oxidation experiments indicates that (i) the measured oscillations of the optical anisotropy are caused by the progression of the local strain pattern during the oxidation, (ii) the oxide layer directly above the interface is disordered and (iii) the oxidation proceeds layer-by-layer and there exists an one-to-one correspondence between the layer oxidation and the inversion of the interface optical anisotropy. The results thus suggest optical spectroscopy for monitoring and controlling the oxidation process with atomic resolution.

Strong modifications of the intramolecular transitions upon adsorption on Si(001) are found even for a molecule like 9,10-phenanthrenequinone, where bonding and functional groups are seemingly decoupled. This shows that a naive interpretation of the surface optical response in terms of molecular transitions fails. On the other hand, the optical anisotropy of the substrate is significantly altered. The total spectrum is dominated by contributions from

adsorption-modified Si bulk states. This indicates that optical spectroscopies may indeed be used to characterize organic-inorganic interfaces.

Our results show the wealth of information contained in the surface optical properties and the potential of state-of-the-art numerical simulations to unearth this information.

Grants of computer time from the Höchstleistungsrechenzentrum Stuttgart and the Leibniz-Rechenzentrum München are gratefully acknowledged.

References

1. R. Del Sole, Solid State Commun. **37**, 537 (1981).
2. F. Manghi, R. Del Sole, A. Selloni, and E. Molinari, Phys. Rev. B **41**, 9935 (1990).
3. P. Hohenberg and W. Kohn, Phys. Rev. **136**, B864 (1964).
4. W. Kohn and L. Sham, Phys. Rev. **140**, A1133 (1965).
5. P. E. Blöchl, Phys. Rev. B **50**, 17953 (1994).
6. G. Kresse and D. Joubert, Phys. Rev. B **59**, 1758 (1999).
7. G. Kresse and J. Furthmüller, Phys. Rev. B **54**, 11169 (1996).
8. J. P. Perdew and A. Zunger, Phys. Rev. B **23**, 5048 (1981).
9. J. P. Perdew, J. A. Chevary, S. H. Vosko, K. A. Jackson, M. R. Pederson, D. J. Singh, and C. Fiolhais, Phys. Rev. B **46**, 6671 (1992).
10. P. Pulay, Chem. Phys. Lett. **73**, 393 (1980).
11. H. J. Monkhorst and J. D. Pack, Phys. Rev. B **13**, 5188 (1976).
12. J. Dabrowski and H.-J. Müssig, *Silicon Surfaces and Formation of Interfaces* (World Scientific, Singapore, 2000).
13. T. Yasuda, S. Yamasaki, M. Nishizawa, N. Miyata, A. Shklyaev, M. Ichikawa, T. Matsudo, and T. Ohta, Phys. Rev. Lett. **87**, 037403 (2001).
14. T. Yasuda, M. Nishizawa, N. Kumagai, S. Yamasaki, H. Oheda, and K. Yamabe, Thin Solid Films **455-456**, 759 (2004).
15. H. Watanabe, K. Kato, T. Uda, K. Fujita, M. Ichikawa, T. Kawamura, and K. Terakura, Phys. Rev. Lett. **80**, 345 (1998).
16. H. Kageshima and K. Shiraishi, Phys. Rev. Lett. **81**, 5936 (1998).
17. T. Nakayama and M. Murayama, Appl. Phys. Lett. **77**, 4286 (2000).
18. A. Incze, R. Del Sole, and G. Onida, Phys. Rev. B **71**, 035350 (2005).
19. W. G. Schmidt, F. Fuchs, A. Hermann, K. Seino, F. Bechstedt, R. Paßmann, M. Wahl, M. Gensch, K. Hinrichs, N. Esser, S. Wang, W. Lu, and J. Bernholc, J. Phys.: Condens. Matter **16**, S4323 (2004).
20. F. Fuchs, W. G. Schmidt, and F. Bechstedt, J. Phys. Chem. B (accepted).
21. T. Yamasaki, K. Kato, and T. Uda, Phys. Rev. Lett. **91**, 146102 (2003).
22. R. Shioda and J. van der Weide, Phys. Rev. B **57**, R6823 (1998).
23. W. G. Schmidt, F. Bechstedt, and J. Bernholc, Phys. Rev. B **63**, 045322 (2001).
24. K. Fujita, H. Watanabe, and M. Ichikawa, Appl. Phys. Lett. **70**, 2807 (1997).
25. C. A. Hacker and R. J. Hamers, J. Phys. Chem. B **107**, 7689 (2003).
26. L. Fang, J. Liu, S. Coulter, X. Cao, M. P. Schwartz, C. Hacker, and R. J. Hamers, Surf. Sci. **514**, 362 (2002).
27. A. Hermann, W. Schmidt, and F. Bechstedt, J. Phys. Chem. B **109**, 7928 (2005).